THE JOURNAL OF PHYSICAL CHEMISTRY C
A JOURNAL OF THE AMERICAN CHEMICAL SOCIETY

pubs.acs.org/JPCC

Article

A ReaxFF Force Field for 2D-WS_2 and Its Interaction with Sapphire

Nadire Nayir, Yun Kyung Shin, Yuanxi Wang, Mert Y. Sengul, Danielle Reifsnyder Hickey, Mikhail Chubarov, Tanushree H. Choudhury, Nasim Alem, Joan Redwing, Vincent H. Crespi, and Adri C. T. van Duin*

Cite This: *J. Phys. Chem. C* 2021, 125, 17950−17961

Read Online

ACCESS | Metrics & More | Article Recommendations | Supporting Information

ABSTRACT: We present a new ReaxFF reactive force field parameter set enabling large-scale computational synthesis and characterization of 2D-WS_2, guided by an extensive quantum mechanical data set on both periodic and nonperiodic systems and validated against ADF-STEM experiments. This potential is designed to capture the most essential features of a WS_2 thin film, such as the 2H → 1T displacive phase transition, S-vacancy migration, and the energetics of various point and line defects, e.g., ripplocations in a WS_2 monolayer, thus enabling cost-effective simulations supporting phase and defect engineering of 2D-WS_2. Additionally, the new ReaxFF description accurately describes the nucleation of a finite 1T phase on the 2H basal plane or edges, the rotational and translational grain boundaries, and the coupled effect of chemical potential and edge stability on the formation of S- and W-oriented grain boundaries. Because the epitaxial relationship between the substrate and 2D flakes plays a key role in controlling the growth direction and thus the crystal quality of a 2D film, this potential is trained further for the WS_2/sapphire interface and therefore can provide valuable insights into the morphological changes observed in a coalesced WS_2 grown film on sapphire.

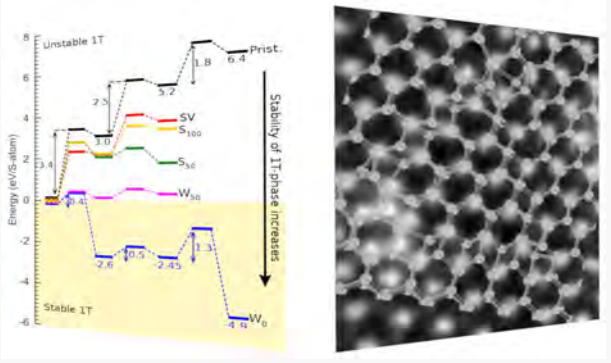

INTRODUCTION

The exfoliation of graphite into a free-standing graphene layer in 2004[1] stimulated research on ultrathin two-dimensional (2D) materials such as h-BN, phosphorene, transition metal dichalcogenides (TMDs), and van der Waals heterostructures thereof.[2−6] The material science community has progressively explored the unique and thickness-dependent properties of 2D materials. Among these, TMDs are regarded as a promising subclass due to their versatile optical, mechanical, and electronic properties spanning from semiconducting to metallic, which motivates pursuit of a wide variety of applications such as electronics, photonics, and energy storage.[6−12] 2D TMDs with the formula MX_2, where M is a transition metal (groups 4−10B) and X is a chalcogen (group 7A), possess distinct and sometimes superior material properties over their bulk counterparts that are composed of layers coupled weakly by van der Waals interlayer forces. Thinning the bulk to monolayer thickness produces an indirect-to-direct band gap transition, band gap size enlargement, increased exciton binding energy, and stronger Coulombic interactions.[12−14] The thickness dependence of TMDs may make it possible to tailor their properties to obtain desirable functionalities for next-generation devices.[15−18]

To date, many experimental studies have focused on the synthesis and characterization of 2D TMD materials by applying various growth and visualization techniques, representing great progress.[19−23] Annular dark-field scanning transmission electron microscopy (ADF-STEM) has been deployed to investigate characteristics of materials on the atomic scale in real time and has provided valuable insights into the atomic structure and dynamics of structural impurities, such as point and line defects.[20,24] These experimental achievements have increased the need for a fundamental understanding of the scalable synthesis and characterization of TMDs. Quantum mechanical (QM) methods have been intensively utilized for the past two decades for the theoretical investigation of TMDs and have provided highly accurate insights into their structural characteristics; however, they are limited to relatively small systems of up to 1000 atoms due to their heavy computational burden. This has stimulated the development of empirical potentials that have become essential to simulate 2D materials at large scales and low computational cost. Empirical potentials can be classified into two groups: nonreactive and reactive force fields. Classical nonreactive

Received: April 21, 2021
Revised: July 25, 2021
Published: August 6, 2021

Downloaded via PENNSYLVANIA STATE UNIV on May 26, 2022 at 10:44:18 (UTC).
See https://pubs.acs.org/sharingguidelines for options on how to legitimately share published articles.

© 2021 American Chemical Society

https://doi.org/10.1021/acs.jpcc.1c03605
J. Phys. Chem. C 2021, 125, 17950−17961

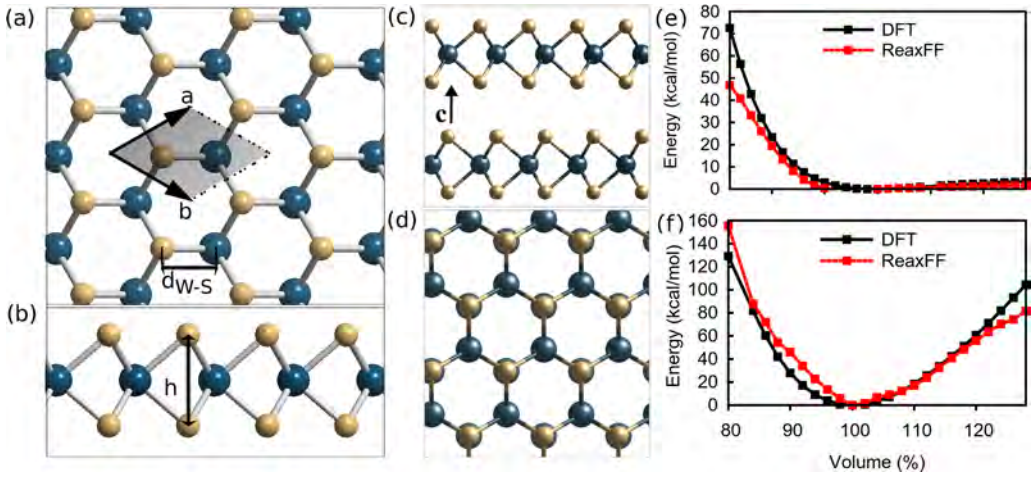

Figure 1. Ball-and-stick representations of (a) the top view and (b) side view of 2H monolayer and (c) the side view and (d) top view of the $2H_c$ bilayer of WS_2. The equations of state of (e) the WS_2 monolayer with uniform in-plane strain and (f) bilayer strained uniaxially along the out-of-plane direction.

empirical potentials (i.e., Lennard-Jones,[25] AMBER,[26] and CHARM[27]) considerably reduce the computational cost. However, such computational methods require the fixed bonded description and thus do not allow bond rupture and formation over the course of the simulation, which prevents an accurate description of chemical events and causes the loss of information. On the other hand, reactive force fields (i.e., Tersoff,[28] Brenner,[29] REBO,[30] and ReaxFF[31,32]) successfully bridge the gap between QM methods and nonreactive potentials and can simulate the full dynamic evolution of chemical systems by employing a bond-order concept.

The REBO[33] and Stillinger–Weber[34−36] empirical potentials have both been proposed for the description of 2D-WS_2. The Stillinger–Weber potential was first parametrized by Jiang et al.[34] and then improved by refs 35 and 36 for W/S interactions. This potential has a simple many-body form including terms that enable the simulation of the nonlinear characteristics of a material, such as thermal conductivity and nonlinear elastic effects at a low computational cost. However, it has difficulty describing nonequilibrium states.[20] The REBO bond-order potential was developed by Han et al.[33] to model WS_2–WSe_2 and MoS_2–WSe_2 heterostructures. Its potential parameters were fit against DFT data including only the lattice parameters of the crystal of interest and the associated stress–strain curve profiles.

Here we report a ReaxFF reactive force field for W/S/H/Al/O interactions to study the computational design and characterization of 2D-WS_2 on a sapphire substrate, trained against QM data on both nonperiodic and periodic systems. This data set contains the formation energies of the semiconducting and metallic phases of 2D-WS_2, point defects, and ripplocations with/without defects as well as the excess energies of edges with different sulfur coverages. The bond-angle energetics of $W(SH)_2S_2$ were also included in the data set. To simulate sapphire/2D-WS_2 interactions, we also considered the formation energies of the corundum-$Al_2O_{3-x}S_x$ structure and various concentrations of sulfur impurities in an Al-fcc crystal as well as the adsorption energy and diffusion barrier for a sulfur atom on the Al(100) and Al(111) surfaces. The accuracy and transferability of the newly developed force field were then validated by benchmark molecular dynamics simulations of various 2D applications and by their comparison with post-training DFT data and ADF-STEM experiments performed for this work as well as the relevant reports from the literature. The details of the force fitting procedure and results, the optimized potential parameters, and the simulation and experimental methods being exploited in this work are presented in the Supporting Information.

THEORETICAL METHOD

ReaxFF developed by van Duin et al.[31] adopts a bond-order concept that is described as a measurement of bond stability between a pair of atoms. The bond order is computed at each iteration of molecular dynamics simulations as the total number of electrons participating in a bond construction. This potential reduces computational cost by describing implicitly the chemical environment and thus enables simulation of large systems up to 1,000,000 atoms over long time scales. ReaxFF has been developed and validated for a wide range of materials such as 2D materials,[37−46] semiconductors,[47,48] and carbon-based materials.[49−52] A detailed description of the ReaxFF formalism can be found in ref 32.

RESULTS AND DISCUSSION

Crystal Stability and 1T → 2H Phase Transition in WS_2 Monolayer. Structural phase transitions are one of the fundamental phenomena in material science and of great interest to technology because the physicochemical properties of a material can be tuned toward desirable functions by atomic displacements. It is well-known that the semiconducting 2H is the most common form of WS_2, and its synthesis is thermodynamically more favorable than that of the metallic 1T phase.[53−55] To test the accuracy of the newly developed ReaxFF potential, we investigated the structural properties of 2H-WS_2 and the 1T → 2H displacive phase transition.

Figure 1a–d shows the atomic structures of free-standing monolayer and bilayer of 2H-WS_2 predicted by ReaxFF and the energy–volume equations of state for a WS_2 monolayer with uniform in-plane strain and bilayer strained uniaxially along the out-of-plane direction (Figure 1e,f). The unit cell of bilayer WS_2 has the $2H_c$ stacking with the space group of $P6_3/mmc$. In this type of the stacking arrangement, the upper layer is rotated by 60° along the out-of-plane direction relative to the lower layer (Figure 1c,d). Their equilibrium values predicted

https://doi.org/10.1021/acs.jpcc.1c03605
J. Phys. Chem. C 2021, 125, 17950−17961

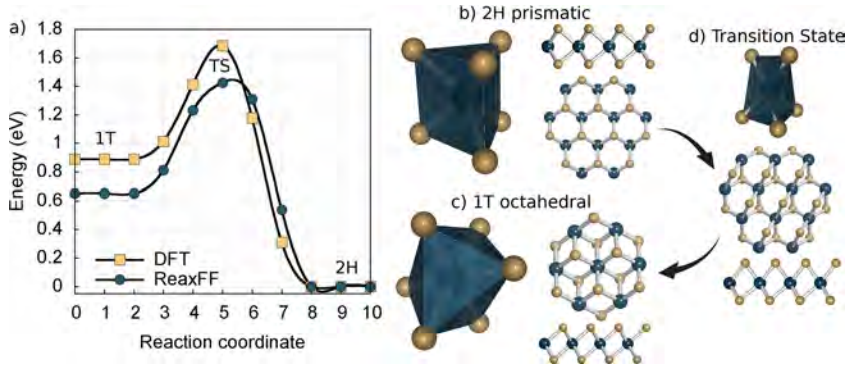

Figure 2. 1T → 2H displacive phase transition. (a) Comparative minimum-energy pathways predicted by ReaxFF and DFT, where the energies (in eV) displayed in the graph are per formula unit of WS_2. The ReaxFF-based optimized atomic configurations of (b) 2H, (c) 1T, and (d) a transition state labeled as TS.

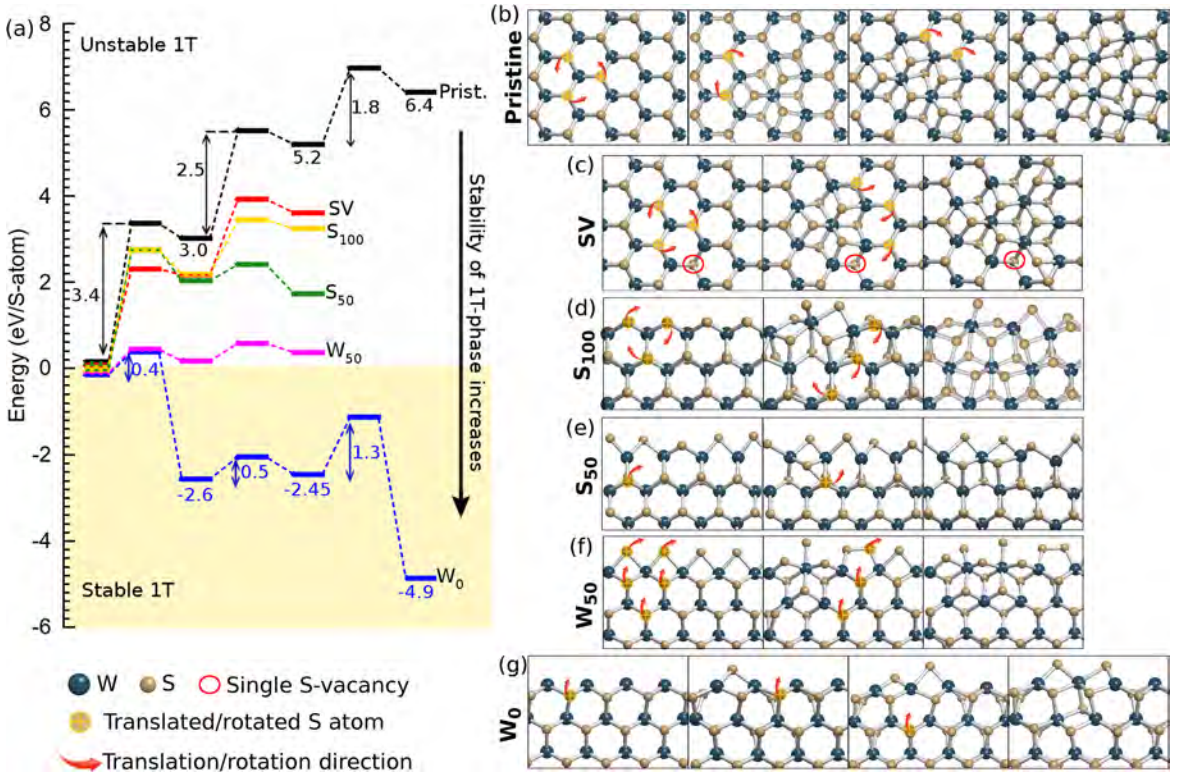

Figure 3. Stepwise transition mechanism of 1T nucleation and propagation in a WS_2 nanosheet. (a) ReaxFF-based reaction and activation energies of 1T formation on models of (b) pristine and (c) SV monolayer and (d) S_{100}, (e) S_{50}, (f) W_{50}, and (g) W_0 edges. In the yellow shaded region in (a), the formation of the 1T phase in the W edge without S coverage, W_0, exhibits an exothermic behavior and is thermodynamically most stable. In the graph, 0 eV/atom refers to six different reference structures. In the SV model in (c), the red circle indicates an S vacancy site. Red arrows and yellow circles in (b−g) highlight the rotated/translated S atoms and the associated translation/rotation directions, respectively.

by ReaxFF are a = 3.16 Å, γ = 120°, d_{W-S} = 2.39 Å, and h = 3.09 Å, in good agreement with the DFT values of a = 3.16 Å, γ = 120°, d_{W-S} = 2.41 Å, and h = 3.15 Å. Additionally, a reasonable agreement of ReaxFF and DFT achieved on the equations of state in Figure 1e,f validates further the capability of the new force field to predict the mechanical properties of WS_2 under tensile strain.

Figure 2a illustrates that the ReaxFF-based phase transition by the lateral translation of an upper S layer—a martensitic phase transformation—shows good agreement with that at the DFT level, where the 2H-prismatic structure (Figure 2b) is most stable with a formation energy of −2.12 and −2.35 eV within ReaxFF and DFT, respectively, followed by the 1-octahedral phase (Figure 2c) with formation energies of −1.47 and −1.36 eV at ReaxFF and DFT levels, as reported in previous works.[53,55] Both DFT and ReaxFF show that a phase transition from the metallic phase to semiconducting 2H is thermodynamically favored. The ReaxFF energy barrier for the 2H-to-1T transition is 1.43 eV, in reasonably good agreement with the DFT value of 1.69 eV. The activation energy for the reverse transition (1T → 2H) predicted by ReaxFF is 0.77 eV within 0.02 eV of the DFT value as shown in Figure 2d. The formation energies are defined as

$$E_f = E_{total} - \mu_W - 2\mu_S \quad (1)$$

https://doi.org/10.1021/acs.jpcc.1c03605
J. Phys. Chem. C 2021, 125, 17950−17961

where E_{total} is the total energy of a perfect 2D-WS_2 unit cell (1 W and 2 S atoms) and μ_W and μ_S are the chemical potentials of W and S atoms, which are determined from a cohesive energy per atom in bulk bcc-W and α-S.

1T-Phase Nucleation on 2H-Basal Plane and Edges. A phase transition between the 2H and 1T phases can arise from rotational and/or translational movements of atoms in a crystal lattice. Several studies have been devoted to elucidating microscopic mechanism of the 2H → 1T phase transition in TMDs, exploring both nucleation and propagation.[56,57] Jin et al.[57] present a detailed atomistic mechanism of the 2H → 1T phase transition in an MoS_2 nanosheet at the DFT level by exploring various transition mechanisms as a combination of rotational and translational movements of only S atoms. They show that the movement of S atoms manifests a thermodynamically and kinetically distinct behavior on the basal plane and edges: the 1T phase nucleates on the basal plane by the rotational movement of three W−S bonds centered on a W atom and propagates by the coupling of translational and further rotational motions of S atoms (path I). However, the transition mechanism on edges follows the collective/single-atom translational movement of S atoms (path II) since the rotational movement of S atoms has a high energy cost regardless of edge type and the percentage of S coverage.

In accord with ref 57, we employed the new ReaxFF potential to explore a stepwise mechanism of the 1T formation on a 2H-WS_2 basal plane and edges with different S coverages through CI-NEB sampling, considering only the thermodynamically favorable atomic mechanisms reported in ref 57 (i.e., path I for basal plane and path II for the edge models). Figure 3a displays the ReaxFF energies of the 1T nucleation and propagation on the following representative models: a 2H-basal plane with or without a single S vacancy, labeled "SV" and "Pristine", respectively (Figure 3b,c), S-terminated zigzag edges with 100% and 50% S coverages, labeled "S_{100}" and "S_{50}" (Figure 3d,e), and W-terminated zigzag edges with 50% and 0% S coverages labeled "W_{50}" and "W_0" (Figure 3f,g).

Similar to the case of an MoS_2 nanosheet,[57] the 1T nucleation on a pristine 2H-WS_2 monolayer initiates with the collective clockwise rotational motions of three sulfur atoms in the upper S layer around the centered W atom by 60°, and then it propagates by the further rotational movements of the S atoms (Figure 3b). Additionally, as marked by a black line in Figure 3a, 1T phase formation on a 2H-pristine basal plane is highly endothermic; that is, the formation energy of the product is higher than that of the parent 2H phase, indicating that the formation of a finite-size 1T-phase domain in a 2H pristine lattice is thermodynamically unfavorable. Additionally, both nucleation and propagation cost a significant energy; hence, the 1T formation in a 2H perfect lattice is likely kinetically hindered, in a similar trend to ref 57. The nucleation step of the 1T formation appears to be the rate-determining step because of its much higher barrier per rotated S atom, 3.4 eV/atom, as compared to that of the propagation steps, 2.5 and 1.8 eV/atom.

Akin to the pristine case, 1T formation on an SV plane requires a higher energy barrier of 2.3 eV/atom for nucleation than for propagation, which has a barrier of 1.75 eV/atom. Nonetheless, introducing a single S vacancy into a nanosheet (Figure 3c) induces a relatively strong interatomic bond between the undercoordinated W and the adjacent S atoms, so that the energy barriers required for both nucleation and propagation become lower than that of the pristine case and stabilize the 1T domain on the 2H plane (marked with a red line in Figure 3a). This suggests that 1T formation may initiate at defects, as reported in the previous MoS_2 work.[11,12]

Our calculations also show that edge termination and S coverage of 2H edges have an evident impact on the formation of a 1T domain. Figure 3a shows that 1T phase formation manifests an exothermic behavior only on the W_0 edge (indicated by a blue line in the yellow shaded region), resulting in a thermodynamically favorable finite-size 1T domain because of the presence of undercoordinated W atoms on the edge. Additionally, the energy barrier required for the nucleation on the W_0 edge system (0.4 eV/atom) is much lower than that of the other representative edge models shown in Figure 3a, indicating that 1T nucleation on the W_0 edge is kinetically most favored. On the other hand, the nucleation of the 1T phase on an S_{100} edge is thermodynamically less likely since the edge W atoms are fully saturated by S atoms. These results suggest that the 1T phase tends to form on less-stable edge structures such as the W_0 edge, in qualitative agreement with the results of previous work on MoS_2.[57,58]

Grain Boundaries. Grain boundaries (GB) are ubiquitous topological line defects observed in WS_2 crystalline films and play a crucial role in modulating material properties.[20,59−63] For example, recent studies reveal the 1D metallic behavior of 60° grain boundaries,[59,63,64] which strongly modify the electronic properties of 2D materials in interesting ways that may contradict the common belief that GBs always have detrimental effects on the optoelectronic properties of crystalline films.[65] Conversely, understanding the strong interplay between crystal growth and grain boundaries in controlling the morphological structure of growth fronts and coalescing grains is vital to fabricating highly single-crystalline films.

The growth front of a 2D-WS_2 domain consists of two distinct zigzag edges, depending on the edge atom termination: either metallic or chalcogen terminated (Figure S9). Additionally, several experimental and theoretical studies have shown that the majority of TMD flakes prefer to be oriented along two favorable angles (0° and 60°) with respect to *c*-plane sapphire due to a relatively strong interfacial interaction between TMD islands and the substrate at these alignments and the fact that both the TMD domain and sapphire exhibit 3-fold symmetry.[66−68] The coalescence of 0°- and 60°-rotated grains produces a mirror twin boundary (MTB) where two equivalent compositions but differently oriented zigzag edges (both metallic and chalcogen) coalesce, as reported in previous works.[66,67,69] In the case of two aligned grains with the same orientation coalescing, metallic and chalcogen edges merge and form a quasi-single-crystalline film.[19,20] Given the significant impact of grain boundaries and grain orientation on material properties, in the following section, we evaluate the quality and transferability of our new potential to the simulation of various rotational and/or translational grain boundaries formed in a 2H-WS_2 monolayer.

60°-Grain Boundaries. Because the hexagonal 2D-WS_2 has 3-fold (i.e., 120°) rotational symmetry, a rotation of 2H-WS_2 by 60° produces its twin, i.e., a lattice of the same symmetry rotated by 180°. The coalescence of a WS_2 lattice with its twin domain generates a 60°-grain boundary line defect or MTB. Here, we examined the stability of various 60°-grain boundaries formed in the 2H phase, following the structures adopted by ref 59. Figure 4a−f illustrates the atomic

https://doi.org/10.1021/acs.jpcc.1c03605
J. Phys. Chem. C 2021, 125, 17950−17961

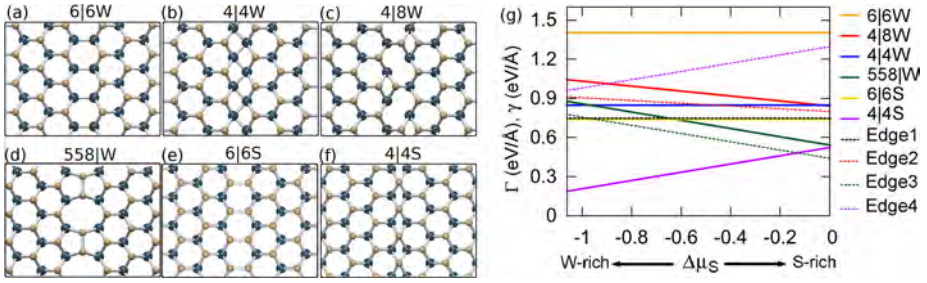

Figure 4. Atomic configurations of (a) 6|6W, (b) 4|4W, (c) 4|8W, (d) 558|S, (e) 6|6S, and (f) 4|4S GBs derived from the various combinations of Edge1, Edge2, Edge3, and Edge4, as depicted in Figure S10. (g) Interface energies of the GBs in (a−f) and the formation energies of Edge1, Edge2, Edge3, and Edge4.

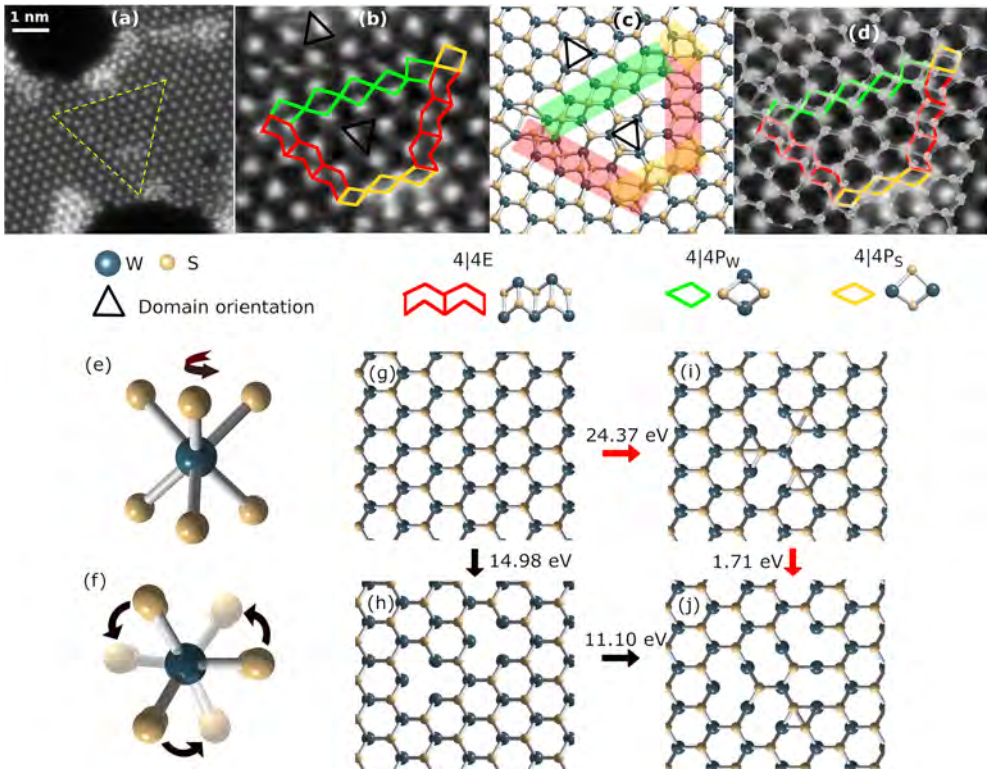

Figure 5. Mirror twin boundaries in a WS_2 monolayer. (a) An ADF-STEM image of MTBs in WS_2 (highlighted with a dashed line). (b) A magnified ADF-STEM image of an MTB formed at the interface of twin domains (inner and outer) with the opposite orientations highlighted with black triangles. (c) ReaxFF-based optimized atomic model of an MTB shown in (b), where yellow balls refer to S atoms and green balls are W atoms. Additionally, the inner domain is framed by 4|4E, 4|4P_S, and 4|4P_W ring formations and is oriented along the opposite direction (black triangle) to the surroundings (outer). (d) A superimposed illustration of the ADF-STEM image in (b) and computed model in (c). (e) The side view and (f) top view of three 60°-rotated W−S bonds centered on a W atom. (g) A perfect lattice of WS_2. (h) Two S divacancies generated in a perfect lattice (i) 3-fold rotational defect generated in a perfect lattice. (j) A defective WS_2 lattice including two divacancies and 3-fold rotational defects. Black arrows indicate the direction of path I (g → h → j), which begins with two divacancies formation in a perfect lattice, and then follows the formation of a 3-fold rotational defect. Path II (g → i → j) is indicated by red arrows, which initiates with a 3-fold rotational defect in a perfect lattice, and then continues with double-divacancy formation.

configurations of the six representative GBs, namely, 6|6W, 4|4W, 4|8W, 558|W, 6|6S, and 4|4S, derived from the various combinations of four different edge types: $Edge_1$, $Edge_2$, $Edge_3$, and $Edge_4$ (Figure S10). In the calculations, a nanoribbon model with the width of L was adopted for both interface and edge excess energy calculations. To prevent spurious interactions between the periodic images, a vacuum with a thickness of 30 Å was inserted along the out-of-plane direction. After minimizing the edge and GB structures, the edge energies of the grains and the interface energies, Γ_{GB}, of the associated GBs were computed via eq 2 as reported in previous works.[58,70]

$$\Gamma_{GB} = \gamma_{G1} + \gamma_{G2} - E_{G1-G2} \quad (2)$$

where γ_{G1} and γ_{G2} are the edge energies of the pristine grains of G_1 and G_2 which are joined into the GB of interest and are determined by using eq S2. E_{G1-G2} is the bonding energy of the interface between the two joined grains, computed as an energy difference between the detached sides and the coalesced system including the grain boundary.

Figure 4g displays the interface energies of the six representative GBs (indicated with solid lines) and the edge energies of the detached edges of each GB (indicated with dashed lines). The structures 6|6W, 4|8W, 4|4W, and 558|W

https://doi.org/10.1021/acs.jpcc.1c03605
J. Phys. Chem. C 2021, 125, 17950−17961

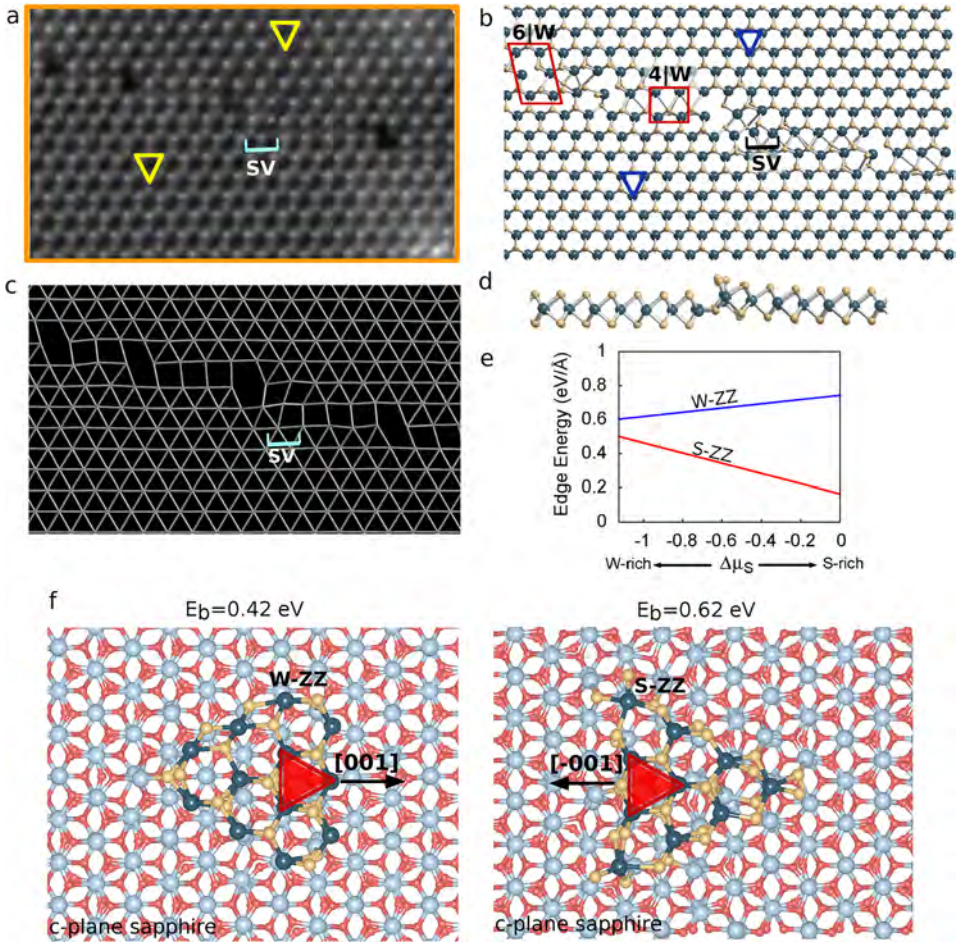

Figure 6. Slanted translational grain boundary in a WS_2 monolayer obtained from experimental ADF-STEM imaging and the ReaxFF simulations. (a) ADF-STEM image showing a slanted grain boundary, the identical in-plane orientation of the upper and lower grains (indicated with yellow triangles), and single vacancy (SV) formation. (b) A ReaxFF model of a slanted grain boundary consisting of 6|W and 4|W rings as well as an SV defect and in-plane-oriented grains (indicated by blue triangle). (c) ReaxFF-based W−W distance maps of the local structure illustrated in (b). (d) Side view of the ReaxFF model shown in (b). (e) Edge formation energies of W-ZZ and S-ZZ as a function of the excess sulfur chemical potential, $\Delta\mu_S$ (in eV) = $\mu_S - \mu_{S(bulk)}$, where $\mu_{S(bulk)}$ is the per-atom energy of bulk alpha-S. (f) ReaxFF-based optimized models of W-ZZ and S-ZZ on an Al-terminated *c*-plane sapphire and the binding energies, E_b (in eV per atom of a WS_2 domain), of W-ZZ and S-ZZ projecting along [001] and [−001] directions on sapphire. Red triangles indicate the orientation of two grains. Both grains manifest the same orientation although their crystallographic growth directions are opposite.

are W-oriented models, and 6|6S and 4|4S GBs are S-oriented models. The structures 6|6W, 4|4W, and 6|6S have the same stoichiometry as a perfect WS_2 lattice; therefore, their edge energies and interface energies do not depend on the sulfur chemical potential. The 4|4S GB is the most stable structure under W-rich conditions and decreases in stability as the environment becomes S-rich. The 6|6W GB in Figure 4a is found to be the thermodynamically least stable conformation with the highest interface energy because of the W−W interaction at the interface at the interface. Of the W-oriented GBs, the 4|4W GB is the most favored GB under W-rich conditions, showing a similar trend with MoS_2 GBs[59] (Figure 4b). Note that the 4|4W model is obtained by shifting one of the grains of 6|6W by half of the W−W bond distance along the GB direction, as described in ref 59.

Mirror Twin Boundary Mediated by 3-Fold Rotated Defects and S Vacancies. To examine the quality of the new force field, we applied it to the MTB formed in a WS_2 monolayer as revealed by the ADF-STEM imaging of Figure 5a,b. In this image, the three W−S bonds centered on W atoms located in an inversion domain (enclosed by a dashed triangular) are rotated by 60° from those in the surrounding region (Figure 5d,e). Similar to the observation reported in previous works,[71−74] the optimized atomic model shows that this MTB accommodates four-membered rings sharing a point (P) and an edge (E), denoted as 4|4P and 4|4E, respectively. The 4|4P rings are also classified into two types depending on whether chalcogen, 4|4P_S, or metal, 4|4P_W, is shared between the rings (Figure 5c). Additionally, as seen from Figure 5b, the W atoms have the same coordination as in the pristine material while the S atoms change their coordination from 3-fold to 4-fold and then to 3-fold, particularly across the GB consisting of 4|4P rings. As shown in Figure S11, such a rearrangement in the atomic positions requires a S-deficient condition which is accompanied by the formation of 3-fold rotational defects as also discussed in refs 71, 73, and 74.

We further investigated the thermodynamic interplay between S vacancies and 3-fold rotational defects. Figure 5g−j shows two potential paths illustrating the nucleation of an MTB. Path I (g → h → j) initiates with the formation of two S divacancies, followed by the 60° in-plane rotation of three W−S bonds around a W atom, and vice versa for path II (g → i →

https://doi.org/10.1021/acs.jpcc.1c03605
J. Phys. Chem. C 2021, 125, 17950−17961

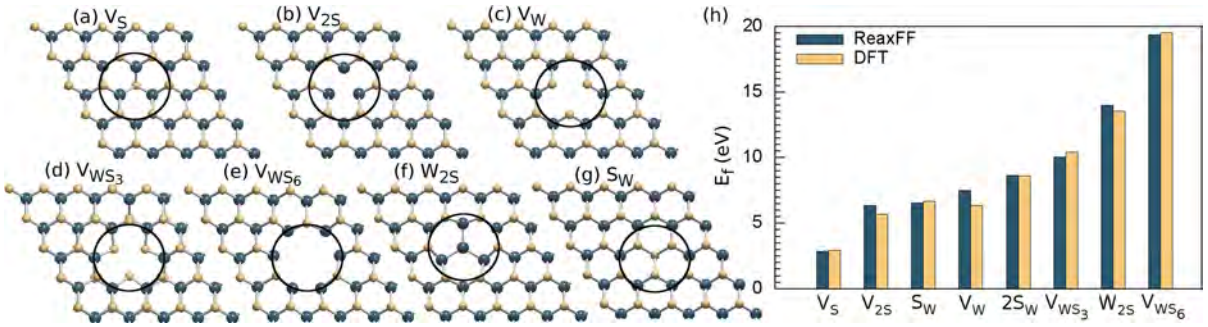

Figure 7. Ball-and-stick representations of the representative point defect models: (a) V_S, (b) V_{2S}, (c) V_W, (d) V_{WS3}, (e) V_{WS6}, (f) W_{2S}, and (g) S_W. (h) Formation energies of the point defects at the ReaxFF and DFT levels.

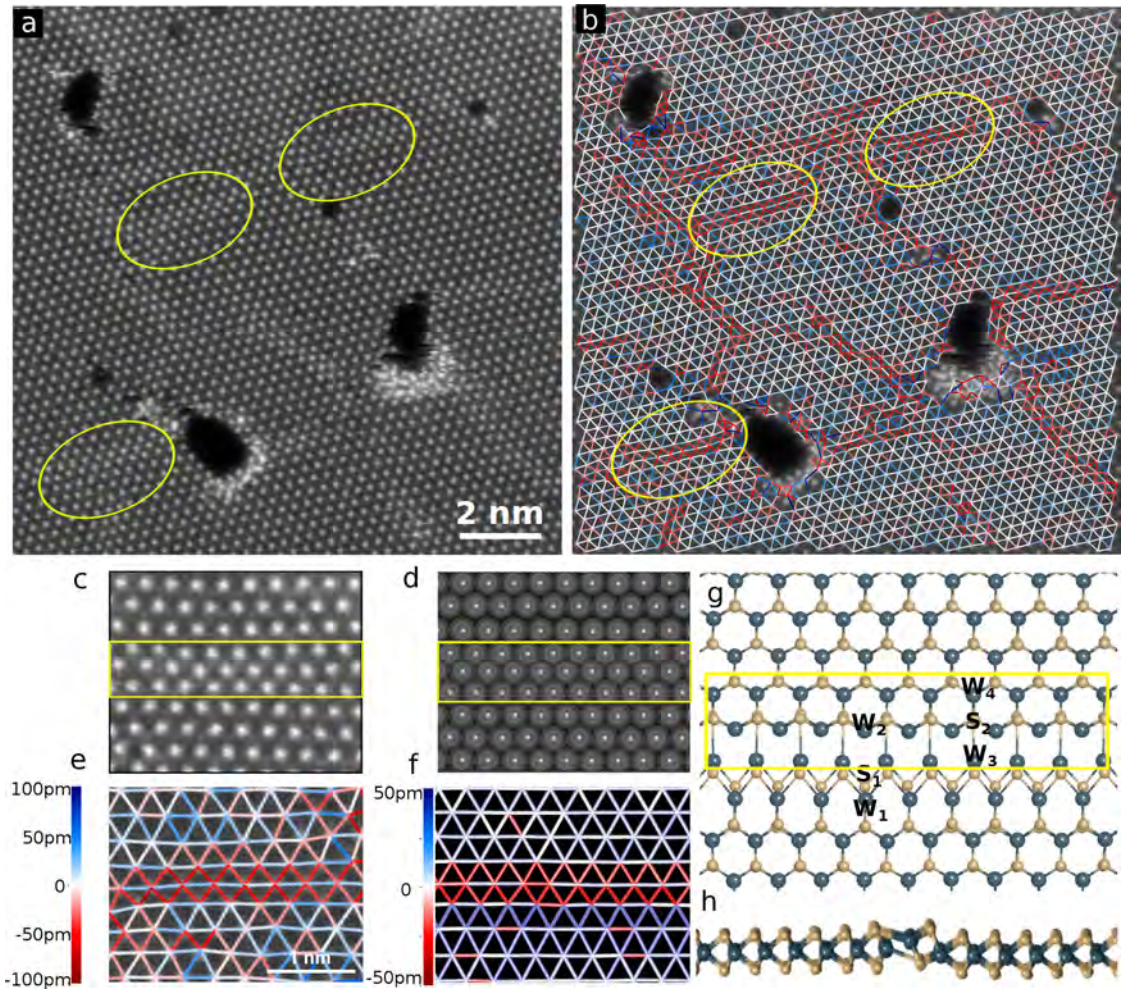

Figure 8. Experimental and ReaxFF-based local structures showing double vacancy line defects in a WS_2 monolayer. (a) An ADF-STEM image showing line defects distributed across a WS_2 monolayer (highlighted with yellow circles). (b) W−W distance map of the ADF-STEM image in (a). (c) A magnified image of region A in (a). (d) Atomic arrangement of only W atoms in the optimized ReaxFF model, where the W−W distances become shortened along the double vacancy line defect (highlighted with a yellow rectangle). (e) Experimental and (f) ReaxFF-based W−W distance maps, where the red lines refer to compression of the lattice and white lines indicate the optimal W−W bond distance in a perfect lattice. (g) Top and (h) side view of the optimized ReaxFF model with a double vacancy line defect indicated with a yellow rectangle.

j). As seen from Figure 5g−j, creating defects such as an S divacancy (Figure 5g → i) and a 3-fold rotational defect in a perfect lattice (Figure 5g → h) is an endothermic process that requires additional energy. Nonetheless, two S divacancies formation with the energy of 14.98 eV is less endothermic and thermodynamically more favorable than that of the 3-fold rotational defect with the energy of 24.37 eV. Additionally, the formation of 3-fold defects in the vicinity of the divacancies (Figure 5h → j) costs lower energy than that in a perfect lattice (Figure 5g → i), indicating S vacancies play a crucial role in the formation of 3-fold rotational defects, which is in good agreement with the results of previous works.[71,73,74] Additionally, once a 3-fold rotational defect forms in a monolayer, two divacancies formation requires only the formation energy of

https://doi.org/10.1021/acs.jpcc.1c03605
J. Phys. Chem. C 2021, 125, 17950−17961

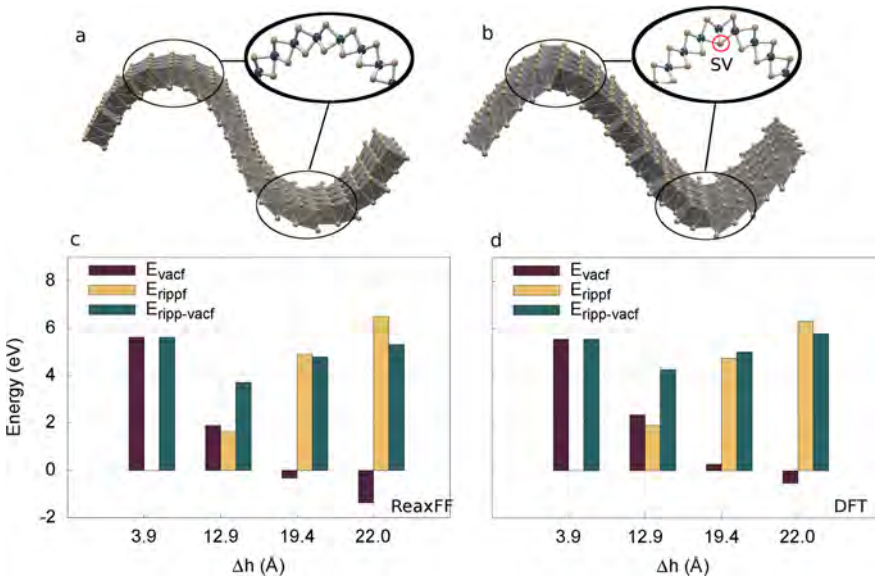

Figure 9. Ripplocations with varying buckling heights. (a) Pristine and (b) defective ripplocations with S vacancies. (c, d) Formation energies of the pristine, E_{rippf}, and defective ripplocations, $E_{ripp\text{-}vacf}$, and a single vacancy, E_{vacf}, at the ReaxFF and DFT levels.

1.71 eV (Figure 5i → j), indicating that a chalcogen vacancy is favored to form in the 3-fold-rotational defect-rich regions.

Slanted Translational Grain Boundary. To test the FF performance for the WS_2/sapphire interface, we investigated the slanted translational grain boundary formed in a coalesced single-orientation WS_2 grown on sapphire, recently reported by Reifsnyder Hickey et al.[20] As investigated by using a combination of ADF-STEM and ReaxFF atomistic simulations, this grain boundary occurs at the interface between two in-plane-oriented grains, in which metal- and chalcogen-terminated edges meet. These boundaries are slanted by various angles between 0° (zigzag) and 30° (armchair), as explained in ref 20. Here we employed the new potential to investigate a slanted translational GB observed in an ADF-STEM image of a WS_2 monolayer as shown in Figure 6a. In line with ref 20, the ReaxFF-computed atomic model in Figure 6b and the W−W distance map in Figure 6c show that the GB consists of 6|W and 4|W rings whose formation is dominated by the underlying sapphire. This results in a translational misalignment between the in-plane-oriented grains by nearly half of the W−W bond distance, ∼1.6 Å. Additionally, the contrast of the S atoms in the upper grain is relatively faint compared to those in the lower grain (Figure 6a) due to the dissimilar edge stabilities of S- and W-terminated grains (Figure 6e). This gives rise to the different binding strengths between each WS_2 domain and *c*-sapphire that evolve over the course of the growth (Figure 6f), consistent with an abrupt change in the atomic positions and tilt along the grain boundary as shown in Figure 6d, in a good agreement with ref 20. Note that studies of WS_2/sapphire interface will be pursued in future work.

Defects in WS_2 Monolayer. *Point Defects.* For the theoretical investigation of defects, ReaxFF is a computationally cost-effective and reliable tool, allowing smooth transitions between bond dissociation and formation over the course of the simulations by creating a reactive chemical environment. To benchmark the performance of this potential to simulate defects in WS_2, we studied the stability of point defects and computed the associated defect formation energies, E_f, using the equation $E_f = E^{defective} - E^{pristine} - n_{Sextra}\mu_S - n_{Wextra}\mu_W$, where $E^{defective}$ and $E^{pristine}$ are the total energies of the defective and pristine free-standing monolayers. Here, μ_S and μ_W represent the chemical potentials of W and S atoms, as determined by the cohesive energy per atom in the corresponding bulk crystals bcc-W and α-S. n_{Sextra} and n_{Wextra} are the number of excess S and W atoms, respectively.

We first modeled a pristine WS_2 sheet containing 108 atoms (72 S and 36 W atoms) using a 6 × 6 hexagonal supercell with the cell dimensions of 14.76 × 14.76 × 20 Å^3, similar to refs 42, 44, and 45, as identified and characterized in previous TMD related experimental work.[75,76] V_S and V_{2S} are single and double S atom vacancies, respectively; V_W is a single W vacancy; V_{WS3} and V_{WS6} represent the absence of a W along with three and six neighboring S atoms in a matrix, respectively. For the antisite models, W_{2s} refers to the replacement of one W atom by a S_2 dimer while the replacements of an S atom and a S_2 dimer by a W atom are called S_w and $2S_w$, respectively. Figure 7h displays the comparative formation energies of these representative point defects based on ReaxFF and DFT. V_S is found to be the thermodynamically most stable point defect, showing good agreement with previous work.[77,78] V_{2S} is the next most stable defect. In contrast, the other vacancies and the antisite defects are thermodynamically unstable as point defects at this choice of chemical potentials.

Sulfur Vacancy Line Defect. As discussed in the previous section, the sulfur vacancy is the thermodynamically most favored point defect and ubiquitously found in WS_2 monolayers as a consequence of either the growth conditions (varying precursor ratio, flow rate, etc.) or irradiation by an electron beam during materials characterization.[77,78] An ADF-STEM image of a WS_2 monolayer in Figure 8a−c,e shows lattice compression along the zigzag direction in the regions highlighted by yellow outlines in Figure 8a,c and red lines in Figure 8b,d. The ReaxFF-based optimized atomic model (Figures 8e) indicates that multiple single S vacancies assemble into a double vacancy line defect comprising two adjacent single vacancy lines. The undercoordinated W atoms relax toward the surrounding S vacancy sites, resulting in relatively short W−W distances in the S-deficient regions, as compared

https://doi.org/10.1021/acs.jpcc.1c03605
J. Phys. Chem. C 2021, 125, 17950−17961

to those in a pristine lattice (Figure 8d,e). The formation of this double vacancy line defect triggers a slight out-of-plane distortion to release the strain accumulated in the defective region (Figure 8h). This phenomenon has been reported in previous works.[20,79] Additionally, the distances between W_1−W_2 and W_3−W_4 are shorter than those in a pristine lattice: 5.12 Å for W_1−W_2 and 4.93 Å for W_3−W_4 as compared to 5.53 Å in the pristine lattice, in a similar trend with ref 81.

Ripplocations. In the same fashion as prior work on WSe_2[44] and $MoSe_2$,[45] we also applied our new potential to a subclass of defects called ripplocations[42,80,81] to examine the interplay between the stability of ripplocations and S-vacancy defects (Figure 9a,b). Following the structures adopted by refs 44 and 45, the three representative ripplocation models with or without an S vacancy were constructed, and the associated formation energies computed by using the equations presented in refs 44 and 45. As seen from Figure 9c,d, the energetics of the defective and defect-free ripplocations at ReaxFF and DFT levels follow a similar trend. The stability of both defective and defect-free ripplocations decreases with increasing buckling height of a ripplocation, Δh. The formation of the defective ripplocation becomes more favorable than that of the defect-free ripplocation because ejecting S atoms from high-curvature regions of the ripplocation, particularly at the buckling height of 22 Å, is exothermic, unlike the pristine case or the case of ripplocations with relatively low buckling height (Figure 9a). Additionally, we can safely deduce from Figure 9c,d and the results of WSe_2 and $MoSe_2$ ripplocations reported in refs 44 and 45 that a WS2 ripplocation is a thermodynamically less stable host matrix than $MoSe_2$ and WSe_2 for chalcogen vacancy formation.

CONCLUSIONS

In summary, we developed a ReaxFF reactive force field parameter set describing W/S/Al/O/H interactions. This potential is designed to capture the fundamental solid-phase phenomena observed in 2D-WS_2 grown on sapphire, such as phase transitions, structural impurities (i.e., grain boundaries, vacancy line defects, point defects, and ripplocations), and the WS_2/sapphire interface at large scales. The benchmark tests of the new force field's performance against the available DFT and experimental data demonstrate that this potential description offers a computationally cost-effective and versatile research tool for the 2D community to study the structural engineering and characterization of 2D-WS_2 and its lattice alignment on a sapphire substrate.

ASSOCIATED CONTENT

Supporting Information

The Supporting Information is available free of charge at https://pubs.acs.org/doi/10.1021/acs.jpcc.1c03605.

ReaxFF reactive force field parameters for W/S/H and DFT and ReaxFF calculations for bond dissociation and valence angle distortion (PDF)

Reactive MD force field parameters (TXT)

AUTHOR INFORMATION

Corresponding Author

Adri C. T. van Duin − *Department of Mechanical Engineering and 2-Dimensional Crystal Consortium (2DCC) Materials Research Institute, The Pennsylvania State University, University Park, Pennsylvania 16802, United States;* orcid.org/0000-0002-3478-4945; Email: acv13@psu.edu

Authors

Nadire Nayir − *Department of Mechanical Engineering and 2-Dimensional Crystal Consortium (2DCC) Materials Research Institute, The Pennsylvania State University, University Park, Pennsylvania 16802, United States; Department of Physics, Karamanoglu Mehmetbey University, Karaman 70000, Turkey;* orcid.org/0000-0002-3621-2481

Yun Kyung Shin − *Department of Mechanical Engineering, The Pennsylvania State University, University Park, Pennsylvania 16802, United States;* orcid.org/0000-0001-8198-001X

Yuanxi Wang − *2-Dimensional Crystal Consortium (2DCC) Materials Research Institute and Department of Physics, The Pennsylvania State University, University Park, Pennsylvania 16802, United States;* orcid.org/0000-0002-0659-1134

Mert Y. Sengul − *Department of Pharmaceutical Sciences, University of Maryland, Baltimore, Maryland 21201, United States;* orcid.org/0000-0002-5309-0316

Danielle Reifsnyder Hickey − *2-Dimensional Crystal Consortium (2DCC) Materials Research Institute and Department of Materials Science and Engineering, The Pennsylvania State University, University Park, Pennsylvania 16802, United States*

Mikhail Chubarov − *Department of Materials Science and Engineering, The Pennsylvania State University, University Park, Pennsylvania 16802, United States;* orcid.org/0000-0002-4722-0321

Tanushree H. Choudhury − *2-Dimensional Crystal Consortium (2DCC) Materials Research Institute and Department of Materials Science and Engineering, The Pennsylvania State University, University Park, Pennsylvania 16802, United States;* orcid.org/0000-0002-0662-2594

Nasim Alem − *2-Dimensional Crystal Consortium (2DCC) Materials Research Institute and Department of Materials Science and Engineering, The Pennsylvania State University, University Park, Pennsylvania 16802, United States;* orcid.org/0000-0003-0009-349X

Joan Redwing − *2-Dimensional Crystal Consortium (2DCC) Materials Research Institute and Department of Materials Science and Engineering, The Pennsylvania State University, University Park, Pennsylvania 16802, United States;* orcid.org/0000-0002-7906-452X

Vincent H. Crespi − *2-Dimensional Crystal Consortium (2DCC) Materials Research Institute and Department of Physics, The Pennsylvania State University, University Park, Pennsylvania 16802, United States*

Complete contact information is available at: https://pubs.acs.org/10.1021/acs.jpcc.1c03605

Notes

The authors declare no competing financial interest.

ACKNOWLEDGMENTS

This work was financially supported by the National Science Foundation (NSF) through the Pennsylvania State University 2D Crystal Consortium−Materials Innovation Platform (2DCC-MIP) under the NSF cooperative agreement DMR1539916. D.R.H. and N.A. acknowledge support from the NSF CAREER program (DMR-1654107). This work

utilized resources provided by the NSF-MRSEC-sponsored Materials Characterization Lab at Penn State (DMR-1420620).

REFERENCES

(1) Novoselov, K. S.; Geim, A. K.; Morozov, S. V.; Jiang, D.; Zhang, Y.; Dubonos, S. V.; Grigorieva, I. V.; Firsov, A. A. Electric Field Effect in Atomically Thin Carbon Films. *Science* **2004**, *306* (5696), 666−669.

(2) Butler, S. Z.; Hollen, S. M.; Cao, L.; Cui, Y.; Gupta, J. A.; Gutiérrez, H. R.; Heinz, T. F.; Hong, S. S.; Huang, J.; Ismach, A. F.; Johnston-Halperin, E.; Kuno, M.; Plashnitsa, V. V.; Robinson, R. D.; Ruoff, R. S.; Salahuddin, S.; Shan, J.; Shi, L.; Spencer, M. G.; Terrones, M.; Windl, W.; Goldberger, J. E. Progress, Challenges, and Opportunities in Two-Dimensional Materials beyond Graphene. *ACS Nano* **2013**, *7* (4), 2898−2926.

(3) Xu, M.; Liang, T.; Shi, M.; Chen, H. Graphene-Like Two-Dimensional Materials. *Chem. Rev.* **2013**, *113* (5), 3766−3798.

(4) Zhang, K.; Feng, Y.; Wang, F.; Yang, Z.; Wang, J. Two Dimensional Hexagonal Boron Nitride (2D-HBN): Synthesis, Properties and Applications. *J. Mater. Chem. C* **2017**, *5* (46), 11992−12022.

(5) Das, S.; Robinson, J. A.; Dubey, M.; Terrones, H.; Terrones, M. Beyond Graphene: Progress in Novel Two-Dimensional Materials and van Der Waals Solids. *Annu. Rev. Mater. Res.* **2015**, *45* (1), 1−27.

(6) Manzeli, S.; Ovchinnikov, D.; Pasquier, D.; Yazyev, O. V.; Kis, A. 2D Transition Metal Dichalcogenides. *Nature Reviews Materials* **2017**, *2* (8), 1−15.

(7) Radisavljevic, B.; Radenovic, A.; Brivio, J.; Giacometti, V.; Kis, A. Single-Layer MoS 2 Transistors. *Nat. Nanotechnol.* **2011**, *6* (3), 147−150.

(8) Splendiani, A.; Sun, L.; Zhang, Y.; Li, T.; Kim, J.; Chim, C.-Y.; Galli, G.; Wang, F. Emerging Photoluminescence in Monolayer MoS2. *Nano Lett.* **2010**, *10* (4), 1271−1275.

(9) Xu, X.; Yao, W.; Xiao, D.; Heinz, T. F. Spin and Pseudospins in Layered Transition Metal Dichalcogenides. *Nat. Phys.* **2014**, *10* (5), 343−350.

(10) Koppens, F. H. L.; Mueller, T.; Avouris, P.; Ferrari, A. C.; Vitiello, M. S.; Polini, M. Photodetectors Based on Graphene, Other Two-Dimensional Materials and Hybrid Systems. *Nat. Nanotechnol.* **2014**, *9* (10), 780−793.

(11) Mak, K. F.; Shan, J. Photonics and Optoelectronics of 2D Semiconductor Transition Metal Dichalcogenides. *Nat. Photonics* **2016**, *10* (4), 216−226.

(12) Mak, K. F.; Lee, C.; Hone, J.; Shan, J.; Heinz, T. F. Atomically Thin ${\mathrm{MoS}}_{2}$: A New Direct-Gap Semiconductor. *Phys. Rev. Lett.* **2010**, *105* (13), 136805.

(13) Zhang, Y.; Chang, T.-R.; Zhou, B.; Cui, Y.-T.; Yan, H.; Liu, Z.; Schmitt, F.; Lee, J.; Moore, R.; Chen, Y.; Lin, H.; Jeng, H.-T.; Mo, S.-K.; Hussain, Z.; Bansil, A.; Shen, Z.-X. Direct Observation of the Transition from Indirect to Direct Bandgap in Atomically Thin Epitaxial MoSe 2. *Nat. Nanotechnol.* **2014**, *9* (2), 111−115.

(14) Sun, Y.; Wang, D.; Shuai, Z. Indirect-to-Direct Band Gap Crossover in Few-Layer Transition Metal Dichalcogenides: A Theoretical Prediction. *J. Phys. Chem. C* **2016**, *120* (38), 21866−21870.

(15) Villaos, R. A. B.; Crisostomo, C. P.; Huang, Z.-Q.; Huang, S.-M.; Padama, A. A. B.; Albao, M. A.; Lin, H.; Chuang, F.-C. Thickness Dependent Electronic Properties of Pt Dichalcogenides. *npj 2D Materials and Applications* **2019**, *3* (1), 1−8.

(16) Synnatschke, K.; Cieslik, P. A.; Harvey, A.; Castellanos-Gomez, A.; Tian, T.; Shih, C.-J.; Chernikov, A.; Santos, E. J. G.; Coleman, J. N.; Backes, C. Length- and Thickness-Dependent Optical Response of Liquid-Exfoliated Transition Metal Dichalcogenides. *Chem. Mater.* **2019**, *31* (24), 10049−10062.

(17) Roldan, R.; Silva-Guillén, J. A.; López-Sancho, M. P.; Guinea, F.; Cappelluti, E.; Ordejon, P. Electronic Properties of Single-Layer and Multilayer Transition Metal Dichalcogenides MX2 (M = Mo, W and X = S, Se). *Ann. Phys.* **2014**, *526* (9−10), 347−357.

(18) Ellis, J. K.; Lucero, M. J.; Scuseria, G. E. The Indirect to Direct Band Gap Transition in Multilayered MoS2 as Predicted by Screened Hybrid Density Functional Theory. *Appl. Phys. Lett.* **2011**, *99* (26), 261908.

(19) Chubarov, M.; Choudhury, T. H.; Hickey, D. R.; Bachu, S.; Zhang, T.; Sebastian, A.; Bansal, A.; Zhu, H.; Trainor, N.; Das, S.; Terrones, M.; Alem, N.; Redwing, J. M. Wafer-Scale Epitaxial Growth of Unidirectional WS2Monolayers on Sapphire. *ACS Nano* **2021**, *15*, 2532−2541.

(20) Reifsnyder Hickey, D.; Nayir, N.; Chubarov, M.; Choudhury, T. H.; Bachu, S.; Miao, L.; Wang, Y.; Qian, C.; Crespi, V. H.; Redwing, J. M.; van Duin, A. C. T.; Alem, N. Illuminating Invisible Grain Boundaries in Coalesced Single-Orientation WS_2 Monolayer Films. *Nano Lett.***2021**.

(21) Choudhury, T. H.; Zhang, X.; Al Balushi, Z. Y.; Chubarov, M.; Redwing, J. M. Epitaxial Growth of Two-Dimensional Layered Transition Metal Dichalcogenides. *Annu. Rev. Mater. Res.* **2020**, *50* (1), 155−177.

(22) Choudhury, T. H.; Simchi, H.; Boichot, R.; Chubarov, M.; Mohney, S. E.; Redwing, J. M. Chalcogen Precursor Effect on Cold-Wall Gas-Source Chemical Vapor Deposition Growth of WS2. *Cryst. Growth Des.* **2018**, *18* (8), 4357−4364.

(23) Choi, W.; Choudhary, N.; Han, G. H.; Park, J.; Akinwande, D.; Lee, Y. H. Recent Development of Two-Dimensional Transition Metal Dichalcogenides and Their Applications. *Mater. Today* **2017**, *20* (3), 116−130.

(24) Mendes, R. G.; Pang, J.; Bachmatiuk, A.; Ta, H. Q.; Zhao, L.; Gemming, T.; Fu, L.; Liu, Z.; Rümmeli, M. H. Electron-Driven In Situ Transmission Electron Microscopy of 2D Transition Metal Dichalcogenides and Their 2D Heterostructures. *ACS Nano* **2019**, *13* (2), 978−995.

(25) Lennard-Jones, J. E. Cohesion. *Proc. Phys. Soc.* **1931**, *43* (5), 461−482.

(26) Weiner, P. K.; Kollman, P. A. AMBER: Assisted Model Building with Energy Refinement. A General Program for Modeling Molecules and Their Interactions. *J. Comput. Chem.* **1981**, *2* (3), 287−303.

(27) MacKerell, A. D.; Bashford, D.; Bellott, M.; Dunbrack, R. L.; Evanseck, J. D.; Field, M. J.; Fischer, S.; Gao, J.; Guo, H.; Ha, S.; Joseph-McCarthy, D.; Kuchnir, L.; Kuczera, K.; Lau, F. T. K.; Mattos, C.; Michnick, S.; Ngo, T.; Nguyen, D. T.; Prodhom, B.; Reiher, W. E.; Roux, B.; Schlenkrich, M.; Smith, J. C.; Stote, R.; Straub, J.; Watanabe, M.; Wiórkiewicz-Kuczera, J.; Yin, D.; Karplus, M. All-Atom Empirical Potential for Molecular Modeling and Dynamics Studies of Proteins. *J. Phys. Chem. B* **1998**, *102* (18), 3586−3616.

(28) Tersoff, J. Empirical Interatomic Potential for Carbon, with Applications to Amorphous Carbon. *Phys. Rev. Lett.* **1988**, *61* (25), 2879−2882.

(29) Brenner, D. W. Empirical Potential for Hydrocarbons for Use in Simulating the Chemical Vapor Deposition of Diamond Films. *Phys. Rev. B: Condens. Matter Mater. Phys.* **1990**, *42* (15), 9458−9471.

(30) Brenner, D. W.; Shenderova, O. A.; Harrison, J. A.; Stuart, S. J.; Ni, B.; Sinnott, S. B. A Second-Generation Reactive Empirical Bond Order (REBO) Potential Energy Expression for Hydrocarbons. *J. Phys.: Condens. Matter* **2002**, *14* (4), 783−802.

(31) van Duin, A. C. T.; Dasgupta, S.; Lorant, F.; Goddard, W. A. ReaxFF: A Reactive Force Field for Hydrocarbons. *J. Phys. Chem. A* **2001**, *105* (41), 9396−9409.

(32) Chenoweth, K.; van Duin, A. C. T.; Goddard, W. A. ReaxFF Reactive Force Field for Molecular Dynamics Simulations of Hydrocarbon Oxidation. *J. Phys. Chem. A* **2008**, *112* (5), 1040−1053.

(33) Han, Y.; Li, M.-Y.; Jung, G.-S.; Marsalis, M. A.; Qin, Z.; Buehler, M. J.; Li, L.-J.; Muller, D. A. Sub-Nanometre Channels Embedded in Two-Dimensional Materials. *Nat. Mater.* **2018**, *17* (2), 129−133.

https://doi.org/10.1021/acs.jpcc.1c03605
J. Phys. Chem. C 2021, 125, 17950−17961

(34) Jiang, J.-W.; Zhou, Y.-P. Parameterization of Stillinger-Weber Potential for Two-Dimensional Atomic Crystals. arXiv:1704.03147 [cond-mat] **2017**. DOI: 10.5772/intechopen.71929.
(35) Susarla, S.; Manimunda, P.; MoraisJaques, Y.; Hachtel, J. A.; Idrobo, J. C.; Syed Amnulla, S. A.; Galvão, D. S.; Tiwary, C. S.; Ajayan, P. M. Deformation Mechanisms of Vertically Stacked WS2 /MoS2 Heterostructures: The Role of Interfaces. *ACS Nano* **2018**, *12* (4), 4036−4044.
(36) Mobaraki, A.; Kandemir, A.; Yapicioglu, H.; Gülseren, O.; Sevik, C. Validation of Inter-Atomic Potential for WS2 and WSe2 Crystals through Assessment of Thermal Transport Properties. *Comput. Mater. Sci.* **2018**, *144*, 92−98.
(37) Osti, N. C.; Naguib, M.; Ostadhossein, A.; Xie, Y.; Kent, P. R. C.; Dyatkin, B.; Rother, G.; Heller, W. T.; van Duin, A. C. T.; Gogotsi, Y.; Mamontov, E. Effect of Metal Ion Intercalation on the Structure of MXene and Water Dynamics on Its Internal Surfaces. *ACS Appl. Mater. Interfaces* **2016**, *8* (14), 8859−8863.
(38) Osti, N. C.; Naguib, M.; Ganeshan, K.; Shin, Y. K.; Ostadhossein, A.; van Duin, A. C. T.; Cheng, Y.; Daemen, L. L.; Gogotsi, Y.; Mamontov, E.; Kolesnikov, A. I. Influence of Metal Ions Intercalation on the Vibrational Dynamics of Water Confined between MXene Layers. *Phys. Rev. Materials* **2017**, *1* (6), 065406.
(39) Sang, X.; Xie, Y.; Yilmaz, D. E.; Lotfi, R.; Alhabeb, M.; Ostadhossein, A.; Anasori, B.; Sun, W.; Li, X.; Xiao, K.; Kent, P. R. C.; van Duin, A. C. T.; Gogotsi, Y.; Unocic, R. R. In Situ Atomistic Insight into the Growth Mechanisms of Single Layer 2D Transition Metal Carbides. *Nat. Commun.* **2018**, *9* (1), 1−9.
(40) Lotfi, R.; Naguib, M.; Yilmaz, D. E.; Nanda, J.; van Duin, A. C. T. A Comparative Study on the Oxidation of Two-Dimensional Ti3C2MXene Structures in Different Environments. *J. Mater. Chem. A* **2018**, *6* (26), 12733−12743.
(41) Mortazavi, B.; Ostadhossein, A.; Rabczuk, T.; van Duin, A. C. T. Mechanical Response of All-MoS2 Single-Layer Heterostructures: A ReaxFF Investigation. *Phys. Chem. Chem. Phys.* **2016**, *18* (34), 23695−23701.
(42) Ostadhossein, A.; Rahnamoun, A.; Wang, Y.; Zhao, P.; Zhang, S.; Crespi, V. H.; van Duin, A. C. T. ReaxFF Reactive Force-Field Study of Molybdenum Disulfide (MoS2). *J. Phys. Chem. Lett.* **2017**, *8* (3), 631−640.
(43) Xuan, Y.; Jain, A.; Zafar, S.; Lotfi, R.; Nayir, N.; Wang, Y.; Choudhury, T. H.; Wright, S.; Feraca, J.; Rosenbaum, L.; Redwing, J. M.; Crespi, V.; van Duin, A. C. T. Multi-Scale Modeling of Gas-Phase Reactions in Metal-Organic Chemical Vapor Deposition Growth of WSe2. *J. Cryst. Growth* **2019**, *527*, 125247.
(44) Nayir, N.; Wang, Y.; Shabnam, S.; Hickey, D. R.; Miao, L.; Zhang, X.; Bachu, S.; Alem, N.; Redwing, J.; Crespi, V. H.; van Duin, A. C. T. Modeling for Structural Engineering and Synthesis of Two Dimensional WSe2 Using a Newly Developed ReaxFF Reactive Force Field. *J. Phys. Chem. C* **2020**, *124* (51), 28285−28297.
(45) Nayir, N.; Wang, Y.; Ji, Y.; Choudhury, T. H.; Redwing, J. M.; Chen, L.-Q.; Crespi, V. H.; van Duin, A. C. T. Theoretical Modeling of Edge-Controlled Growth Kinetics and Structural Engineering of 2D-$MoSe_2$. *Mater. Sci. Eng., B* **2021**, *271*, 115263.
(46) Rajabpour, S.; Mao, Q.; Nayir, N.; Robinson, J.; van Duin, A. C. T. Development of a ReaxFF Reactive Force Field for Ga/C/H and In/C/H Interactions. *J. Phys. Chem. C* **2021**, *125* (19), 10747−10758.
(47) Nayir, N.; Van Duin, A. C. T.; Erkoc, S. Development of a ReaxFF Reactive Force Field for Interstitial Oxygen in Germanium and Its Application to GeO2/Ge Interfaces. *J. Phys. Chem. C* **2019**, *123* (2), 1208−1218.
(48) Nayir, N.; Van Duin, A. C. T.; Erkoc, S. Development of the 954 ReaxFF Reactive Force Field for Inherent Point Defects in the Si/955 Silica System. *J. Phys. Chem. A* **2019**, *123*, 4303−4313.
(49) Rajabpour, S.; Mao, Q.; Gao, Z.; KhajehTalkhoncheh, M.; Zhu, J.; Schwab, Y.; Kowalik, M.; Li, X.; van Duin, A. C. T. Lowtemperature carbonization of polyacrylonitrile/graphene carbon fibers: A combined ReaxFF molecular dynamics and experimental study. *Carbon* **2021**, *174*, 345−356.
(50) Kowalik, M.; Ashraf, C.; Damirchi, B.; Akbarian, D.; Rajabpour, S.; van Duin, A. C. T. Atomistic Scale Analysis of the Carbonization Process for C/H/O/N-Based Polymers with the ReaxFF Reactive Force Field. *J. Phys. Chem. B* **2019**, *123*, 5357−5367.
(51) Zhang, L.; Kowalik, M.; Gao, Z.; Ashraf, C. M.; Rajabpour, S.; Bumgardner, C.; Schwab, Y.; Damirchi, B.; Zhu, J.; Akbarian, D.; et al. Converting PBO Fibers into Carbon Fibers by Ultrafast Carbonization. *Carbon* **2020**, *159*, 432−442.
(52) Mao, Q.; Rajabpour, S.; Kowalik, M.; van Duin, A. C. T. Predicting cost-effective carbon fiber precursors: Unraveling the functionalities of oxygen and nitrogen-containing groups during carbonization from ReaxFF simulations. *Carbon* **2020**, *159*, 25−36.
(53) Hu, Z.; Zhang, S.; Zhang, Y.-N.; Wang, D.; Zeng, H.; Liu, L.-M. Modulating the Phase Transition between Metallic and Semiconducting Single-Layer MoS2 and WS2 through Size Effects. *Phys. Chem. Chem. Phys.* **2015**, *17* (2), 1099−1105.
(54) Toh, R. J.; Sofer, Z.; Luxa, J.; Sedmidubský, D.; Pumera, M. 3R Phase of MoS2 and WS2 Outperforms the Corresponding 2H Phase for Hydrogen Evolution. *Chem. Commun.* **2017**, *53* (21), 3054−3057.
(55) Reale, F.; Palczynski, P.; Amit, I.; Jones, G. F.; Mehew, J. D.; Bacon, A.; Ni, N.; Sherrell, P. C.; Agnoli, S.; Craciun, M. F.; Russo, S.; Mattevi, C. High-Mobility and High-Optical Quality Atomically Thin WS 2. *Sci. Rep.* **2017**, *7* (1), 1−10.
(56) Zhao, W.; Ding, F. Energetics and Kinetics of Phase Transition between a 2H and a 1T MoS 2 Monolayer—a Theoretical Study. *Nanoscale* **2017**, *9* (6), 2301−2309.
(57) Jin, Q.; Liu, N.; Chen, B.; Mei, D. Mechanisms of Semiconducting 2H to Metallic 1T Phase Transition in Two-Dimensional MoS2 Nanosheets. *J. Phys. Chem. C* **2018**, *122* (49), 28215−28224.
(58) Zou, X.; Yakobson, B. I. An Open Canvas—2D Materials with Defects, Disorder, and Functionality. *Acc. Chem. Res.* **2015**, *48* (1), 73−80.
(59) Zou, X.; Yakobson, B. I. Metallic High-Angle Grain Boundaries in Monolayer Polycrystalline WS2. *Small* **2015**, *11* (35), 4503−4507.
(60) Chen, J.; Jung, G. S.; Ryu, G. H.; Chang, R.-J.; Zhou, S.; Wen, Y.; Buehler, M. J.; Warner, J. H. Atomically Sharp Dual Grain Boundaries in 2D WS2 Bilayers. *Small* **2019**, *15* (42), 1902590.
(61) Azizi, A.; Zou, X.; Ercius, P.; Zhang, Z.; Elías, A. L.; Perea-López, N.; Stone, G.; Terrones, M.; Yakobson, B. I.; Alem, N. Dislocation Motion and Grain Boundary Migration in Two-Dimensional Tungsten Disulphide. *Nat. Commun.* **2014**, *5* (1), 1−7.
(62) Zhou, Y.; Sarwat, S. G.; Jung, G. S.; Buehler, M. J.; Bhaskaran, H.; Warner, J. H. Grain Boundaries as Electrical Conduction Channels in Polycrystalline Monolayer WS2. *ACS Appl. Mater. Interfaces* **2019**, *11* (10), 10189−10197.
(63) Zou, X.; Liu, Y.; Yakobson, B. I. Predicting Dislocations and Grain Boundaries in Two-Dimensional Metal-Disulfides from the First Principles. *Nano Lett.* **2013**, *13* (1), 253−258.
(64) Lahiri, J.; Lin, Y.; Bozkurt, P.; Oleynik, I. I.; Batzill, M. An Extended Defect in Graphene as a Metallic Wire. *Nat. Nanotechnol.* **2010**, *5* (5), 326−329.
(65) Seto, J. Y. W. The Electrical Properties of Polycrystalline Silicon Films. *J. Appl. Phys.* **1975**, *46* (12), 5247−5254.
(66) Dumcenco, D.; Ovchinnikov, D.; Marinov, K.; Lazić, P.; Gibertini, M.; Marzari, N.; Sanchez, O. L.; Kung, Y.-C.; Krasnozhon, D.; Chen, M.-W.; Bertolazzi, S.; Gillet, P.; Fontcuberta i Morral, A.; Radenovic, A.; Kis, A. Large-Area Epitaxial Monolayer MoS2. *ACS Nano* **2015**, *9* (4), 4611−4620.
(67) Suenaga, K.; Ji, H. G.; Lin, Y.-C.; Vincent, T.; Maruyama, M.; Aji, A. S.; Shiratsuchi, Y.; Ding, D.; Kawahara, K.; Okada, S.; Panchal, V.; Kazakova, O.; Hibino, H.; Suenaga, K.; Ago, H. Surface-Mediated Aligned Growth of Monolayer MoS2 and In-Plane Heterostructures with Graphene on Sapphire. *ACS Nano* **2018**, *12* (10), 10032−10044.
(68) Dong, J.; Zhang, L.; Dai, X.; et al. The epitaxy of 2D materials growth. *Nat. Commun.* **2020**, *11*, 5862.
(69) Zhou, W.; Zou, X.; Najmaei, S.; Liu, Z.; Shi, Y.; Kong, J.; Lou, J.; Ajayan, P. M.; Yakobson, B. I.; Idrobo, J.-C. Intrinsic Structural

Defects in Monolayer Molybdenum Disulfide. *Nano Lett.* **2013**, *13* (6), 2615−2622.
(70) Liu, Y.; Bhowmick, S.; Yakobson, B. I. BN White Graphene with "Colorful" Edges: The Energies and Morphology. *Nano Lett.* **2011**, *11* (8), 3113−3116.
(71) van der Zande, A. M.; Huang, P. Y.; Chenet, D. A.; Berkelbach, T. C.; You, Y.; Lee, G.-H.; Heinz, T. F.; Reichman, D. R.; Muller, D. A.; Hone, J. C. Grains and Grain Boundaries in Highly Crystalline Monolayer Molybdenum Disulphide. *Nat. Mater.* **2013**, *12* (6), 554−561.
(72) Zhou, W.; Zou, X.; Najmaei, S.; Liu, Z.; Shi, Y.; Kong, J.; Lou, J.; Ajayan, P. M.; Yakobson, B. I.; Idrobo, J.-C. Intrinsic Structural Defects in Monolayer Molybdenum Disulfide. *Nano Lett.* **2013**, *13* (6), 2615−2622.
(73) Lin, Y.-C.; Björkman, T.; Komsa, H.-P.; Teng, P.-Y.; Yeh, C.-H.; Huang, F.-S.; Lin, K.-H.; Jadczak, J.; Huang, Y.-S.; Chiu, P.-W.; Krasheninnikov, A. V.; Suenaga, K. Three-Fold Rotational Defects in Two-Dimensional Transition Metal Dichalcogenides. *Nat. Commun.* **2015**, *6* (1), 6736.
(74) Komsa, H.-P.; Krasheninnikov, A. V. Engineering the Electronic Properties of Two-Dimensional Transition Metal Dichalcogenides by Introducing Mirror Twin Boundaries. *Advanced Electronic Materials* **2017**, *3* (6), 1600468.
(75) Lin, Z.; Carvalho, B. R.; Kahn, E.; Lv, R.; Rao, R.; Terrones, H.; Pimenta, M. A.; Terrones, M. Defect Engineering of Two-Dimensional Transition Metal Dichalcogenides. *2D Mater.* **2016**, *3* (2), 022002.
(76) Wei, J.; Ma, Z.; Zeng, H.; Wang, Z.; Wei, Q.; Peng, P. Electronic and optical properties of vacancy-doped WS_2 monolayers. *AIP Adv.* **2012**, *2*, 042141.
(77) Hong, J.; Hu, Z.; Probert, M.; Li, K.; Lv, D.; Yang, X.; Gu, L.; Mao, N.; Feng, Q.; Xie, L.; Zhang, J.; Wu, D.; Zhang, Z.; Jin, C.; Ji, W.; Zhang, X.; Yuan, J.; Zhang, Z. Exploring Atomic Defects in Molybdenum Disulphide Monolayers. *Nat. Commun.* **2015**, *6* (1), 6293.
(78) Zhu, Q.; Chen, W.; Cheng, H.; Lu, Z.; Pan, H. WS2 Nanosheets with Highly-Enhanced Electrochemical Activity by Facile Control of Sulfur Vacancies. *ChemCatChem* **2019**, *11* (11), 2667−2675.
(79) Wang, S.; Lee, G.-D.; Lee, S.; Yoon, E.; Warner, J. H. Detailed Atomic Reconstruction of Extended Line Defects in Monolayer MoS2. *ACS Nano* **2016**, *10* (5), 5419−5430.
(80) Kushima, A.; Qian, X.; Zhao, P.; Zhang, S.; Li, J. Ripplocations in van Der Waals Layers. *Nano Lett.* **2015**, *15* (2), 1302−1308.
(81) Barsoum, M. W.; Zhao, X.; Shanazarov, S.; Romanchuk, A.; Koumlis, S.; Pagano, S. J.; Lamberson, L.; Tucker, G. J. Ripplocations: A Universal Deformation Mechanism in Layered Solids. *Phys. Rev. Materials* **2019**, *3* (1), 013602.

https://doi.org/10.1021/acs.jpcc.1c03605
J. Phys. Chem. C 2021, 125, 17950−17961